Journal of Catalysis 421 (2023) 252–263

Contents lists available at ScienceDirect

Journal of Catalysis

journal homepage: www.elsevier.com/locate/jcat

Theoretical study of the mechanism of the hydrogen evolution reaction on the V_2C MXene: Thermodynamic and kinetic aspects

Martí López [a], Kai S. Exner [b,c,d,*], Francesc Viñes [a,*], Francesc Illas [a]

[a] Departament de Ciència de Materials i Química Física & Institut de Química Teòrica i Computacional (IQTCUB), Universitat de Barcelona, c/ Martí i Franqués 1-11, Barcelona 08028, Spain
[b] University Duisburg-Essen, Faculty of Chemistry, Theoretical Inorganic Chemistry, Universitätsstraße 5, 45141 Essen, Germany
[c] Cluster of Excellence RESOLV, Bochum, Germany
[d] Center for Nanointegration (CENIDE) Duisburg-Essen, Duisburg, Germany

ARTICLE INFO

Article history:
Received 16 January 2023
Revised 8 March 2023
Accepted 15 March 2023
Available online 22 March 2023

Keywords:
V_2C
MXene
Density functional calculations
Hydrogen evolution reaction
Kinetics
Tafel plots

ABSTRACT

Both experimentally and theoretically, the MXene family has shown promising hydrogen evolution reaction (HER) capabilities. However, so far, the theoretical approach has been relying on the well-known thermodynamic descriptor, ΔG_H, whereas experimental studies report Tafel plots, containing kinetic rather than thermodynamic information. Aiming to link theory to experiments, the present study explores five different HER pathways over the exemplary V_2C (0001) MXene by density functional theory calculations. While the surface coverage under HER conditions (with either H* or OH* adsorbates) is extracted from a Pourbaix diagram, we determine the energetics of the reaction intermediates and transition states for both surface species as active sites. This enables the construction of free-energy diagrams for the Volmer-Heyrovsky and Volmer-Tafel mechanisms and allows for the simulation of Tafel plots by a rigorous microkinetic framework. While the active-site motif V_2C-OH seems to be less relevant for the HER under typical reaction conditions, we demonstrate that the HER is kinetically facile on the V_2C-H surface. For this surface termination, we report a potential-depending switching of the preferred mechanism from the Volmer-Heyrovsky to the Volmer-Tafel description with increasing overpotential while encountering similarities to the HER over Pt.

© 2023 The Author(s). Published by Elsevier Inc. This is an open access article under the CC BY license (http://creativecommons.org/licenses/by/4.0/).

1. Introduction

Our society is demanding an urgent socioeconomic transformation to face the many issues arising from forthcoming climate emergencies [1–4]. The increasing energetic demand [5] together with the necessity of reducing our dependency on fossil fuels drives the scientific and technological community to look for environmentally sustainable alternatives [6,7]. Among all the alternative energy sources, the use of molecular hydrogen has attracted a considerable attention due to its multiple capabilities in energy storage or for its direct usage replacing the nowadays employed fossil fuels [8–10]. Water splitting is a key reaction towards the production of green hydrogen, where the hydrogen evolution (HER) and oxygen evolution (OER) reactions take place at the cathode and anode of an electrolyzer, respectively [11–13]. However, these technologies still present few setbacks for their large scale application. Currently, the scarce and expensive Pt- and Ir/Ru-based materials are among the best catalysts for HER [14,15] and OER [16], respectively, and consequently, materials based on non-scarce metals are called for to replace Pt- and Ir/Ru-based materials [17].

Currently, materials based on earth-abundant elements are being tested as alternatives to Pt-based catalysts for HER, such as transition-metal carbides (TMCs) and nitrides (TMNs) [18–20] transition-metal sulphides [21–23], phosphides [24–26], or metallic organic frameworks (MOFs) [27] such as Ni-THT [28], Co-BHT, and Co-THT [29]. Among them, a new family of 2D materials, named MXenes [30], is raising considerable expectation [31]. While MXenes are strongly related to TMCs and TMNs in terms of composition, they are structurally very different as MXenes contain a few atomic layers only [32]. Most MXenes adhere to the general formula $M_{n+1}X_n$, where M stands for a metal, usually an early transition metal from groups IV to VI (M = Ti, Zr, Hf, V, Nb, Ta, Cr, Mo, W...) while X stands for carbon or nitrogen. Depending on the synthesis, the surfaces of MXenes are functionalized with groups such as -O, –OH, -H, and -F, and these are normally referred to as

* Corresponding authors.
E-mail addresses: kai.exner@uni-due.de (K.S. Exner), francesc.vines@ub.edu (F. Viñes).

https://doi.org/10.1016/j.jcat.2023.03.027
0021-9517/© 2023 The Author(s). Published by Elsevier Inc.
This is an open access article under the CC BY license (http://creativecommons.org/licenses/by/4.0/).

$M_{n+1}X_nT_x$, where T_x indicates the termination on both metal surfaces of each MXene sheet. In addition, there are new members of the family involving different metals [33] and even MXenes have been proposed where metal and C and N layers can alternate [34]. Meanwhile, MXenes have multiple applications in batteries [35,36], as supercapacitors [37], in antibacterial activity [38], in CO_2 abatement technologies [39–42], and for multiple electrocatalytic processes [43] such as the HER, but also equally discussed as electrocatalysts for the OER [44,45].

Relating to the HER activity of MXenes, Seh *et al.* [46] investigated the suitability of the broadly used Gibbs free energy of hydrogen adsorption, ΔG_H [47], to evaluate the electrocatalytic performance of several O-terminated early transition metal MXenes, such as Sc_2CO_2, $V_3C_2O_2$, Cr_2CO_2, Mo_2CO_2, $Mo_4C_3O_2$, Cr_2NO_2, Nb_2NO_2. Subsequent studies explored an even wider range of MXenes, also addressing the HER activity of these materials [48–51]. In particular, Ling *et al.* [48] proposed the net charge on the atom(s) directly interacting with adsorbed H as an alternative descriptor, yet this charge is indeed dependent on the MXene T_x termination, as already mentioned. Additionally, the effect of termination on HER activity has been studied in detail by Hondoko *et al.* [52] pointing out that F-terminated MXenes tend to exhibit a lower HER catalytic activity than the O-terminated counterparts [52]. This led to identify the exposed terminal O as the active sites of the HER over MXenes [53], suggesting that freshly exfoliated MXenes are not active catalysts for the HER and that some surface functionalization is needed.

Despite the considerable number of studies that aim to comprehend the HER activity of MXenes, including the most recent review [44], so far all theoretical studies rely on thermodynamic considerations only, thus neglecting the effect of the kinetics in the HER. However, the thermodynamic approach may not suffice to explain experimental results in all cases, particularly not if the tacit precondition of Brønsted – Evans – Polanyi relation, which couples the thermodynamic to the kinetic picture, is violated [54–56]. In the present work we present a comprehensive study where, for the first time, the kinetics of the HER over V_2C, taken as an exemplary case of the MXene family, is accounted for besides the thermodynamic picture. This is achieved by the coupling of first-principles calculations in the density functional theory (DFT) approximation, including the determination of transition states, with microkinetic considerations to simulate Tafel plots that can be compared to experiments, a methodology successfully applied in the study of HER over metal oxide systems [57].

2. Surface models and computational approach

The V_2C (0001) basal surface is modelled by a $p(3\times3)$ supercell with three atomic layers stacked in ABC fashion, as in previous works on similar MXenes, see Fig. 1 [39,40,58–60]. The upper and lower layers contain just V atoms whereas C atoms are placed in the middle layer. A vacuum width of around 12 Å along the z direction is added to the supercell to avoid interaction between interleaved MXenes; this is a technicality arising from the use of a computational code that exploits periodic boundary conditions. The surface termination of the V_2C MXene is chosen by inspecting the corresponding Pourbaix diagram as obtained from theoretical calculations [44]. While most works consider a single surface termination only, a recent study considering various adsorbates, including mixed phases [61], showed that the most stable surface coverage is predicted to contain $^2/_3$ and $^1/_3$ of surface sites having adsorbed O* and OH* ($^2/_3$O* + $^1/_3$OH*), respectively under HER conditions, in all cases with adsorbates on their most stable HollowM adsorption sites. Accordingly, this surface phase has been adopted as the starting model to explore the HER kinetics. Nevertheless, only when an overpotential is applied, a turnover in terms of hydrogen formation is observed. In the case of V_2C, at an applied electrode potential of –0.5 V *vs.* the reversible hydrogen electrode (RHE), the most stable surface is fully covered by adsorbed H*, again on HollowM, and this surface phase is included as second model in our study. We also considered the case with full OH* coverage even if a previous work suggests that this situation is not thermodynamically favoured at any pH or potential conditions [61]. This is because, most often, the simulated surface Pourbaix diagrams do not account for the effect of the surrounding solvent. Therefore, to account for the aqueous electrochemical environment, we have added six molecules of water to the surface of the ($^2/_3$O* + $^1/_3$OH*) phase. The atomic structure of the adsorbed water is reminiscent of the ice-like structure, which has already been successfully applied to study the HER kinetics in other systems [62,63]. The explicit water molecules layer includes one extra

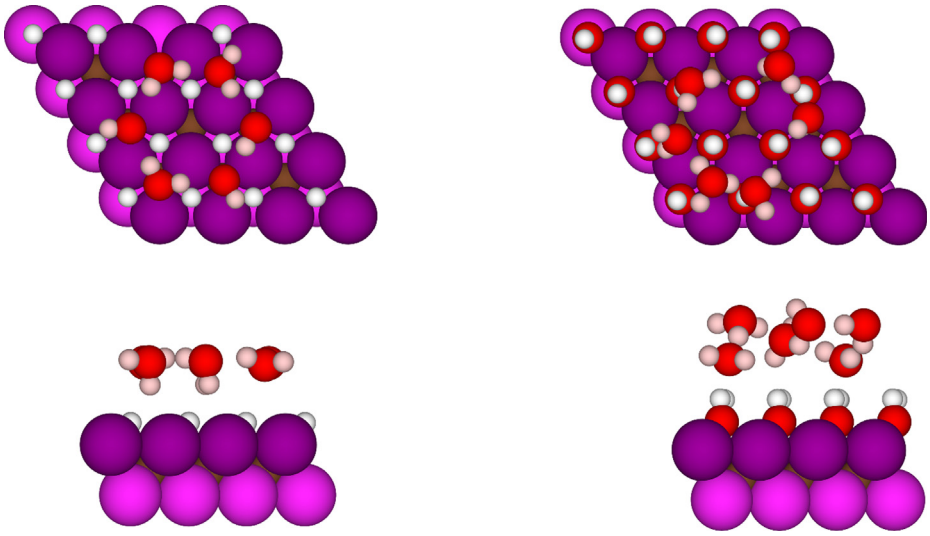


Fig. 1. Top and side views of the $p(3\times3)$ supercells used to represent a V_2C (0001) basal surface terminated by H (left) and OH (right) with the surface covered by six water molecules in an ice-shaped structure. Metal atoms at the top and bottom layers are represented by bright and light purple spheres, while C atoms are represented by dark brown spheres. H atoms adsorbed on the surface and on the water layer are shown as white and pink spheres, respectively, with O atoms shown as red spheres. (For interpretation of the references to colour in this figure legend, the reader is referred to the web version of this article.)

hydrogen, *i.e.* a H_3O moiety, to prompt the H adsorption. In the computational models with the initial ($^2/_3O^* + {}^1/_3OH^*$) surface coverage, this leads to a new situation where the surface is fully covered with OH* groups, and this is the reason why the HER kinetics over the fully OH*-covered surface is investigated in the present study as well.

The present theoretical study of the HER kinetics and reaction mechanisms over V_2C is based on calculations carried out in the framework of density functional theory (DFT) [64,65] using the Vienna *ab-initio* simulation package (VASP) [66–68]. The Perdew-Burke-Erzenhof (PBE) form of the exchange–correlation potential was used [69] including dispersion effects through the Grimme's D3 approach [70]. The electronic density of the valence electrons was expanded using a plane-wave basis set with an energy cut off of 415 eV. The effect of the core electrons on the valence electron density is accounted for through the projector augmented wave (PAW) approach of Blöchl [71], as implemented in VASP by Kresse and Joubert [72]. A value of 10^{-5} eV was set as a convergence criterion for the electronic energy optimization together with a threshold of 0.01 $Å^{-1}$ for the atomic forces acting on every single atom of the system. For the calculations, the partial occupancies of the orbitals are considered by the tetrahedron method with Blöchl corrections. Consequently, a Γ-centered **k**-mesh of $5\times5\times1$ dimensions was used to sample the Brillouin zone for the numerical integration in the reciprocal space. At convergence, the total energy was extrapolated to 0 K. Spin polarization was not considered as no magnetism was reported for V_2C [73–75], and spin polarization has negligible impact on the reaction profiles of non-magnetic materials [76]. Nevertheless, test calculations for the reaction profile relevant structure revealed that, even starting from a spin-polarization trial density, the variational self-consistent field procedure always converges to the closed shell, non-spin polarized solution.

To locate the transition state (TS) structures along the possible reaction paths, we used the climbing-image nudged elastic band [77] (CI-NEB) and the improved dimer method [78], depending on each single geometrical structure. All the identified TS were characterized by proper frequency analysis, carried out by Hessian matrix construction and diagonalization. We used finite displacements of 0.03 Å in length, verifying that in each case, only one imaginary frequency was present. The structures of interest displayed in this work were represented using the VESTA code [79].

3. Hydrogen evolution reaction mechanism

Strongly acidic solutions are preferably used to carry out the HER, although it is occasionally examined in buffered solutions with an intermediate *p*H or under alkaline conditions. Considering the ice-like water layer as a proton donor, we refer to the acidic HER equilibrium:

$$2H^+ + 2e^- \rightleftharpoons H_2, \quad U^0 = 0V \ vs.\ RHE \tag{1}$$

Here we assume a H^+ activity of one, corresponding to *p*H = 0. Note, however that HER performance may vary as a function of *p*H [80], yet the HER is found to be more sluggish at higher *p*H values. Indeed, on Pt reference electrode, low *p*H has been found to favor a Tafel-step control of the kinetics, while higher *p*H favors Volmer-step control, see below.

Two reaction mechanisms are frequently discussed in the literature, denoted as Volmer-Heyrovsky (VH) and Volmer-Tafel (VT) [81,82]; their representation is given in Fig. 2. Both mechanisms have in common that hydrogen is adsorbed on the electrode within the electrochemical Volmer (*cf.* Eq. (2)), but they differ in the second step. In the VH mechanism, the Heyrovsky step is also of electrochemical nature (*cf.* Eq. (3)), in that the adsorbed hydrogen species recombines with another proton from the electrolyte solution to release a single H_2 molecule. On the contrary, the VT mechanism consists of two subsequent Volmer steps and the Tafel step of Eq. (4), a chemical recombination step of the two adjacent hydrogen adsorbates to form H_2.

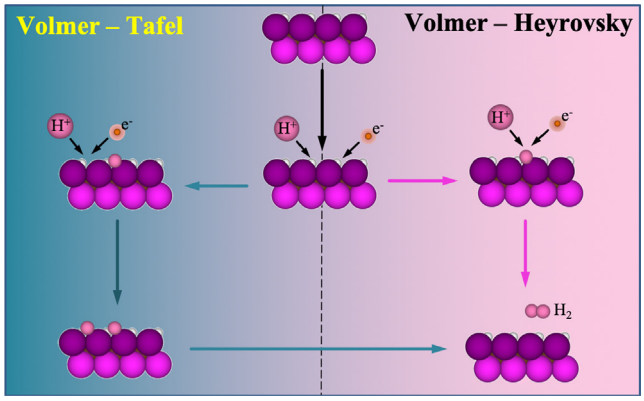


Fig. 2. Schematic view of the two main HER mechanisms. The cycle with green arrows corresponds to the Volmer-Tafel (VT) mechanism whereas orange arrows refer to the description of Volmer-Heyrovsky (VH). Note that the first step, starting on the top of each cycle is the same for both VT and VH, but the formation of H_2 in the VT mechanism is of chemical nature whereas it is an electrochemical step in the VH pathway. Adsorbed H atoms, H^+ ions, and electrons are depicted by white, pink, and red spheres, respectively, while the rest of the colour coding is specified in Fig. 1. (For interpretation of the references to colour in this figure legend, the reader is referred to the web version of this article.)

$$Volmer\ step: \quad H^+ + e^- + * \ \rightarrow \ H*, \tag{2}$$

$$Heyrovsky\ step: \quad H^+ + e^- + H* \ \rightarrow \ * + \ H_2, \tag{3}$$

$$Tafel\ step: \quad 2H* \ \rightarrow \ * + \ H_2 \tag{4}$$

Given that our V_2C surface models under HER conditions contain already adsorbed hydrogen atoms, some additional considerations are needed. As such, the HER can also proceed starting with the Heyrovsky step to produce H_2 using the surface hydrogen without needing an initial Volmer step. Table 1 describes the sequence of steps for the HER mechanisms examined in the current study, employing the two alternative terminations mentioned above and the same line of thought. Nonetheless, based on the terminations considered, not all the mechanisms resulting from combining these steps are allowed. For instance, in the H-terminated MXene (T_x = H), a H from the water layer can bond the metal V Top site and thus any mechanism starting with a Volmer step will be allowed. However, the hydrogen atoms absorbed at HollowM sites that are present in the initial termination are strongly adsorbed (*i.e.* ΔG = -1.05 eV). Consequently, these H atoms cannot be used as a hydrogen source for the HER, and therefore, mechanisms starting with a Heyrovsky or Tafel step cannot proceed and are not considered (*cf.* Fig. 3). In contrast, on the fully OH-terminated V_2C surface, the V Top sites are sterically blocked by the OH groups, thus leaving no free adsorption sites for the H atoms. In contrast to the case of the V_2C-H surface, the mechanisms cannot start with a Volmer step. On the other hand, the H atoms from the surface OH groups are exposed and can be combined to one hydrogen from the water layer *via* one Heyrovsky step or, alternatively, can form a H_2 molecule with another H from the surface OH *via* one Tafel step as schematically shown in Fig. 3. We would like to emphasize that the approximation of the ice-like water layer as hydrogen source on top of the V_2C surface requires caution and, instead of referring

Table 1
Description of the five HER mechanisms over V_2C considered in the present study. The mechanism column defines the label for the studied Volmer-Heyrovsky (VH) and Volmer-Tafel (VT) mechanisms. The last three columns correspond to the order of the steps for each pathway.

MXene	Mechanism	Step I	Step II	Step III
V_2C-H	VH-I	Volmer Step	Heyrovsky Step	
	VT-I	Volmer Step	Volmer Step	Tafel Step
	VT-II	Volmer Step	Tafel Step	Volmer Step
V_2C-OH	VH-II	Heyrovsky Step	Volmer Step	
	VT-III	Tafel Step	Volmer Step	Volmer Step

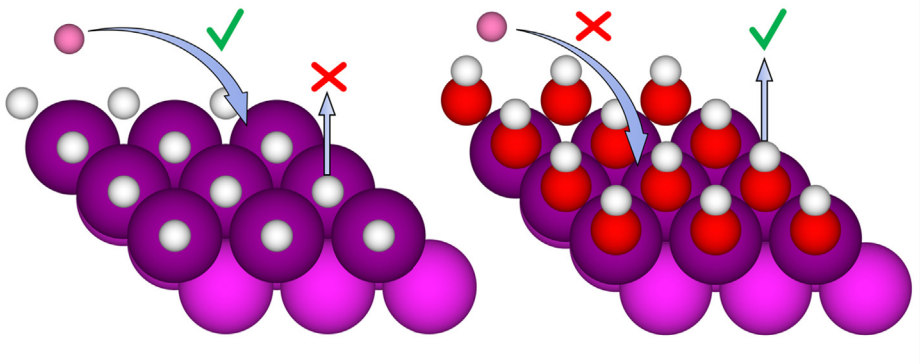


Fig. 3. Schematic representation of the initial steps for the HER that are possible for the H* and OH* terminated V_2C surface. In case of the V_2C-H surface (left image), the Volmer step is the first one because incoming H (shown in pink) can be adsorbed on a vacant surface site (Top). However, the Heyrovsky and Tafel steps are forbidden as the first step because hydrogen at the surface (HollowM) is adsorbed too strongly (*e.g.* ΔG = -1.05 eV). On the contrary, for the V_2C-OH surface (right image), the adsorption sites for H adsorption are sterically blocked by the OH adsorbates on the HollowM position, and consequently, the Volmer step is restrained. Therefore, the mechanistic cycle starts with the release of gaseous hydrogen from the OH groups by a Heyrovsky or a Tafel step. (For interpretation of the references to colour in this figure legend, the reader is referred to the web version of this article.)

to the lowest energy path, we investigated a representative number of options and computed the free-energy diagrams using an average over these paths to reduce possible artifacts.

To finally predict the most favourable mechanism, the free-energy diagrams of all the elementary steps and mechanisms are estimated as indicated in the below. Fig. 4 depicts an example of the free-energy diagram for the conventional VH and VT mechanisms at η = 0 V and 0.2 V over the V_2C-H example; for simplicity, we refer to the absolute value of the HER overpotential in the following even though cathodic overpotentials are formally negative. The free-energy landscape of the HER is directly affected by an increase in the applied overpotential, and the free energies of the reaction intermediates (RI) and transition states are lowered in dependence of the number of electrons (n) transferred according to Eq. (5) and Eq. (6). In the case of TS, the charge transfer between the two involved states is considered not to be complete, which is characterized by the transfer coefficient, α. Its specific value is usually unknown but for a one-electron transfer step, such as encountered with the Volmer and Heyrovsky steps, α is approximated to be $^1/_2$ based on experimental evidence of HER performance on Pt [83], and a usual choice [84].

$$\Delta G(\eta) = \Delta G(0) - (n \cdot e \cdot \eta), \tag{5}$$

$$\Delta G^{\#}(\eta) = \Delta G^{\#}(0) - [(n + \alpha) \cdot e \cdot \eta]. \tag{6}$$

In equations (5) and (6), $\Delta G(\eta)$ and $\Delta G(0)$ denote the free-energy changes from the initial state (*e.g.*, starting surface) to the final state (*e.g.*, reaction intermediate or product H_2) at zero overpotential or any arbitrary η value, respectively. Similarly, $\Delta G^{\#}$ is the free-energy change from the initial state to a TS, and n or e indicate the number of electrons transferred or the elementary charge, respectively. Based on this framework, the free-energy profile of the VH mechanism is modified in such a way that the Gibbs free energy of TS #$_1$ is reduced by $\alpha_1 \cdot e \cdot \eta$ and that of RI by $1 \cdot e \cdot \eta$, TS #$_2$ is lowered by $(1 + \alpha_2) \cdot e \cdot \eta$ and the product state by $2 \cdot e \cdot \eta$, see Fig. 4a. In a similar way, for the free-energy profile corresponding to the VT mechanism, the first steps are equally affected in that the values for #$_1$ is reduced by $\alpha_1 \cdot e \cdot \eta$, that of RI1 by $1 \cdot e \cdot \eta$, that of #$_2$ by $(1+\alpha_2) \cdot e \cdot \eta$, while for RI2, #$_3$, and the product state the Gibbs free energy is reduced by $2 \cdot e \cdot \eta$, as no more electrons are transferred in the Tafel step, see Fig. 4b.

Recent works on the free-energy landscape in electrocatalysis have demonstrated that not the highest free-energy barrier, $\Delta G^{\#}$, but rather the TS with the highest free energy, $G^{\#}_{rds}$, governs the kinetics of the overall reaction [74,85 74]. For the HER, $G^{\#}_{rds}$ is either given by the free-energy difference between TS #$_1$ and the starting surface ($G^{\#}_1$) or between TS #$_2$ and the starting surface ($G^{\#}_2$). As such, the free-energy barriers in the free-energy diagram corresponding to the Volmer-Heyrovsky mechanism are related to the respective TS free energies in Eqs. (7) and (8):

$$G^{\#}_1 = \Delta G^{\#}_1, \tag{7}$$

$$G^{\#}_2 = \Delta G^{\#}_2 + \Delta G_{RI}. \tag{8}$$

Inspecting the free-energy profile of Fig. 4a, it turns out that $G^{\#}_2$ corresponds to $G^{\#}_{rds}$ at η = 0 V whereas $G^{\#}_1$ is met with $G^{\#}_{rds}$ at η = 0.2 V. Similarly, for the VT free-energy profile one can define $G^{\#}_1$, $G^{\#}_2$, and $G^{\#}_3$ by referring to Eqs. (9)-(11);

$$G^{\#}_1 = \Delta G^{\#}_1, \tag{9}$$

$$G^{\#}_2 = \Delta G^{\#}_2 + \Delta G_{RI1}, \tag{10}$$

$$G^{\#}_3 = \Delta G^{\#}_3 + \Delta G_{RI2}. \tag{11}$$

Fig. 4b reveals that $G^{\#}_3$ and $G^{\#}_1$ are encountered with $G^{\#}_{rds}$ at η = 0 V and η = 0.2 V, respectively.

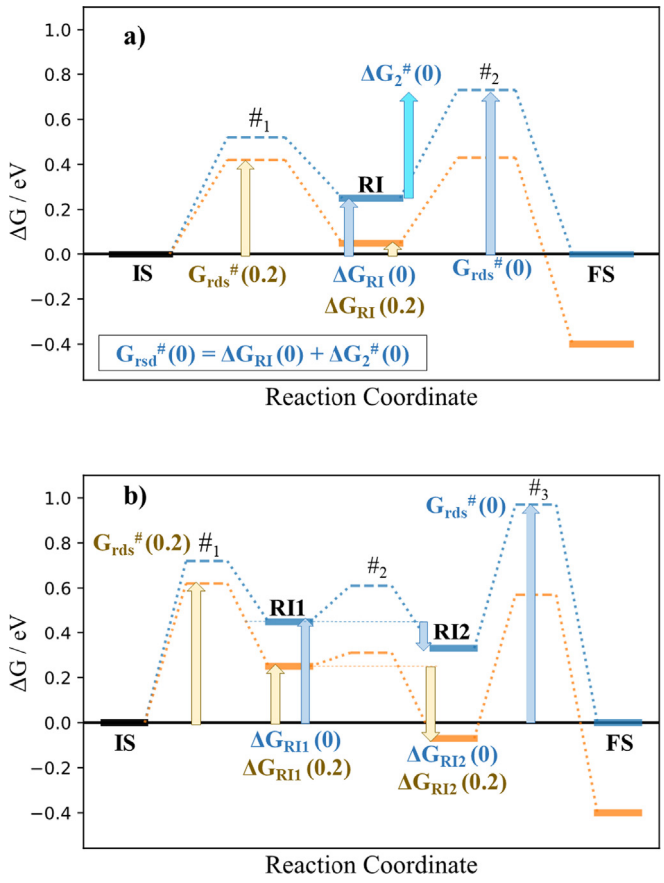


Fig. 4. Schematic representation of an arbitrarily chosen Gibbs free energy profile based on the V_2C-H model for the a) Volmer-Heyrovsky and b) Volmer-Tafel mechanisms at η = 0 V and η = 0.2 V in blue and orange, respectively. The initial state (IS) is depicted in black. The final state (FS) and the reaction intermediate (RI) are depicted by a solid line while transition states (TSs) are marked as $\#_n$ (n = 1, 2) by dashed lines. $G_{RIx}(0)$ and $G_{RIx}(0.2)$ are the corresponding free energies for the reaction intermediate at η = 0 V and η = 0.2 V, respectively. $G^{\#}_{rds}(0)$ and $G^{\#}_{rds}(0.2)$ correspond to the transition state with highest free energy in dependence of the applied overpotential. Finally, $\Delta G^{\#}_2$ in light blue corresponds to the barrier of the second elementary step in panel a). (For interpretation of the references to colour in this figure legend, the reader is referred to the web version of this article.)

4. Computational construction of Tafel plots

Tafel plots indicate the rate of an electrochemical reaction, estimated from the current density, in dependence of the applied overpotential, serving as the driving force for the process. Commonly, a logarithmic plot is used in that the $\log_{10}$ of the current density, j, is applied. This finding can be traced to the Tafel equation, which can be derived as approximation for sufficiently large overpotentials from the Butler-Volmer theory [85,86]:

$$\log_{10} j(\eta) = \log_{10} j_0 + \frac{\eta}{b}, \tag{12}$$

where $j(\eta)$ and j_0 are the current density as a function of the overpotential η, and the exchange current density, respectively, and b denotes the Tafel slope. The Tafel slope contains information about the transfer coefficient which plays an important role for the reaction kinetics relating to the TS (*cf.* Eq. (6)).

While the analysis and interpretation of Tafel plots can offer valuable insight into the elementary reaction steps and kinetics, it is not straightforward to translate the energetic picture in terms of the free-energy landscape (*cf.* Fig. 4) into a Tafel plot. This requires several assumptions which are discussed in the following. The first aspect refers to the description of the RI coverage. The two common approximations refer to the quasi-equilibrium and steady-state assumptions. The quasi-equilibrium approximation, based on thermodynamic considerations in terms of the law of mass action, assumes that the coverage of the RI remains essentially constant upon increasing overpotential, and thus, the quasi-equilibrium model is only a good choice if coverages are not prone to change. Yet, it was demonstrated that quasi-equilibrium is a valid approximation if there is a single linear regime in the Tafel plot [77]. In case of the steady-state approximation, the RI coverage is described by the rate constants (kinetics) of the elementary steps, thereby taking alterations in the RI concentration on the electrode surface with increasing overpotential into account. Considering the VH mechanism as depicted in Fig. 3a, the time-dependent RI concentration as a function of the applied overpotential is described by Eq. (13):

$$\left(\frac{d([RI])}{dt}\right)_{\eta} = k_1(\eta)\cdot[IS] + k_{-2}(\eta)\cdot[FS] - k_{-1}(\eta)\cdot[RI] - k_2(\eta)\cdot[RI], \tag{13}$$

which is deduced from the elementary steps of Eqs. (14) and (15):

$$IS \underset{k_{-1}}{\overset{k_1}{\rightleftharpoons}} RI \tag{14}$$

$$RI \underset{k_{-2}}{\overset{k_2}{\rightleftharpoons}} FS \tag{15}$$

In the above equations, $k_1(\eta)$ and $k_{-1}(\eta)$ are the forward and backward rate constants of the elementary step in Eq. 14; equally, $k_2(\eta)$ and $k_{-2}(\eta)$ correspond to the forward and backward rate constants of the step in Eq. 15. [IS], [FS], and [RI] are the concentrations of the initial state, final state, and the reaction intermediate, respectively. We would like to emphasize that we omitted the activity of the reactant (H^+) in the microkinetic expression of Eq. 13. This is due to the assumption of a^+_H = 1, *vide supra*, emphasizing that our model is dedicated to the HER kinetics in acidic conditions.

Please note that depending on the surface configuration of V_2C (*cf.* Table 1), the IS can be either a metal atom, *, or adsorbed hydrogen, *-H. This renders whether the RI corresponds to *-H or * + H_2, respectively.

Given that all the RIs within the HER are adsorbed species, we can relate their concentrations to their coverage at the electrode surface. In this context, we redefine [IS] and [FS] as θ_S, and [RI] as θ_{S-H}, where θ_S and θ_{S-H} correspond to the coverage of vacant sites or the coverage of adsorbed hydrogen on the MXene surface. Considering the balance of active sites and the steady-state approximation, the two conditions of Eq. (16) and Eq. (17) must be fulfilled.

$$\left(\frac{d([RI])}{dt}\right)_{\eta} = 0, \tag{16}$$

$$\theta_S(\eta) + \theta_{S-H}(\eta) = 1, \tag{17}$$

where the definition or reaction rate is

$$r(\eta) = \frac{d[H_2]}{dt} = k_2(\eta)\cdot\theta_{S-H}(\eta) - k_{-2}(\eta)\cdot\theta_S(\eta). \tag{18}$$

With this, one can rewrite the reaction rate expression in Eq. (13) as;

$$r(\eta) = \frac{k_1(\eta)\cdot k_2(\eta)}{k_1(\eta)+k_{-1}(\eta)+k_2(\eta)+k_{-2}(\eta)} - \frac{k_{-1}(\eta)\cdot k_{-2}(\eta)}{k_1(\eta)+k_{-1}(\eta)+k_2(\eta)+k_{-2}(\eta)}. \tag{19}$$

Finally, we apply Faraday's law to obtain the current density in dependence of the applied overpotential:

$$j(\eta) = n \cdot e \cdot r(\eta) \cdot \Gamma_{act}. \tag{20}$$

The substitution of the expression of r(η) in Eq. (19) into Eq. (20) leads, after some algebra, to Eq. (21). We additionally make use of the assumption that only the forward reaction is accounted for in the Tafel regime (η > 0.03 V) [87], because the overpotential applied is large enough to fairly neglect the backward reaction.

$$j(\eta) = \frac{2k_B T e \Gamma_{act}}{h} \cdot \frac{exp\left(\frac{(\alpha_1+\alpha_2)\eta e}{k_B T}\right)}{exp\left(\frac{G_1^{\#}+\alpha_2\eta e}{k_B T}\right) + exp\left(\frac{G_2^{\#}-(1-\alpha_1)\eta e}{k_B T}\right) + exp\left(\frac{G_2^{\#}-\Delta G_{RI}+\alpha_1\eta e}{k_B T}\right)}, \tag{21}$$

where k_B is Boltzmann's constant, T the temperature in Kelvin, h is Planck's constant, e is the elementary charge, Γ_{act} is the density of active sites in cm^{-2}, defined as $\Gamma_{act} = \frac{n^{\circ}\text{ of sites}}{\text{surface area}}$, α_1 and α_2 are the transfer coefficients of the first and second steps, $G_1^{\#}$ and $G_2^{\#}$ are the TS free energies of the first and second step (*cf.* equations (7) and (8)), and finally, ΔG_{RI} corresponds to the free energy of the reaction intermediate at η = 0. In order to facilitate the calculations and to compare them to experimental values, j(η) is not expressed in the international system units but in A/cm^{-2}. Please note that the evaluation of Eq. (21) requires knowledge of both the energetics of the thermodynamics and kinetics in terms of ΔG and $\Delta G^{\#}$, respectively. Based on the evaluation of Eq. (21), it becomes possible to simulate Tafel plots in dependence of the applied overpotential and to correlate the Tafel lines to the rate-determining step, as obtained from free-energy diagrams (*cf.* Fig. 4).

However, for reactions with more steps as VT, the steady-state assumption requires a more complex expression since more RIs are involved. Yet, the quasi-equilibrium approach offers a simple alternative to simulate the Tafel plot for the VT mechanism. While the quasi-equilibrium approximation is not able to capture the transitions between linear Tafel regimes, indicating a change in the rate-determining step of the reaction, it can fairly estimate each linear region individually [88]. Thus, by applying the quasi-equilibrium analysis to each TS allows obtaining three linear regimes, and the least favourable regime is reconciled with the rate-determining step in dependence of the applied overpotential, see Fig. 5.

The preceding discussion illustrates that the simulation of Tafel plots requires the knowledge of various quantities, such as ΔG and $G_s^{\#}$ for the RIs and TSs, respectively. These terms are obtained by DFT calculations, analysing the difference in Gibbs free energies for each individual steps. At zero overpotential, ΔG_{RI}, $\Delta G_1^{\#}$ and $\Delta G_2^{\#}$ are obtained from Eq. (21):

$$\Delta G = \Delta E_{TOT} + \Delta E_{ZPE} - T\Delta S \tag{22}$$

For a free-energy change between two intermediate states, ΔG_{RI}, ΔE_{TOT} refers to the energy difference between the initial and final states whereas for the free-energy barriers $\Delta G_1^{\#}$ and $\Delta G_2^{\#}$, ΔE_{TOT} correspond to the energy difference between the initial state and the first or the RI and second TS, respectively. In general, for processes involving n steps the total free-energy difference from n-1 to n is obtained according to Eq. (23) and (24) for RIs and TSs, respectively.

$$\Delta E_{TOT} = E_n - E_{n-1}, \tag{23}$$

or,

$$\Delta E_{TOT}^{\#} = E_n^{\#} - E_{n-1} \tag{24}$$

In Eq. (22), ΔE_{ZPE} corresponds to the zero-point energy difference between two consecutive steps, n-1 and n. In the present study we computed the ΔE_{ZPE} for the two different surfaces in a slightly different way. For V_2C-H we assume that the vibrations of the water layer and the H adsorbate involved in the RIs are decoupled from the vibrations of the MXene, including the H layer of the termination. Therefore, the frequencies taken explicitly into account are those from the extra H and of the water layer. However, for the V_2C-OH surface, the vibrations of the OH from the MXene termination are accounted for. The reason for such difference is the nature of the RIs involved on the different MXenes. In the case of V_2C-H, the H involved in the RIs are adsorbed on V Top site, and the vibrations can be safely decoupled from those of the rest of the MXene, including the termination. However, in the case of V_2C-OH, the RIs directly involve the H atoms form the OH termination and thus, they must be included. Therefore, the ΔE_{ZPE} term is computed within the harmonic approximation, as given in Eqs. (25) and (26);

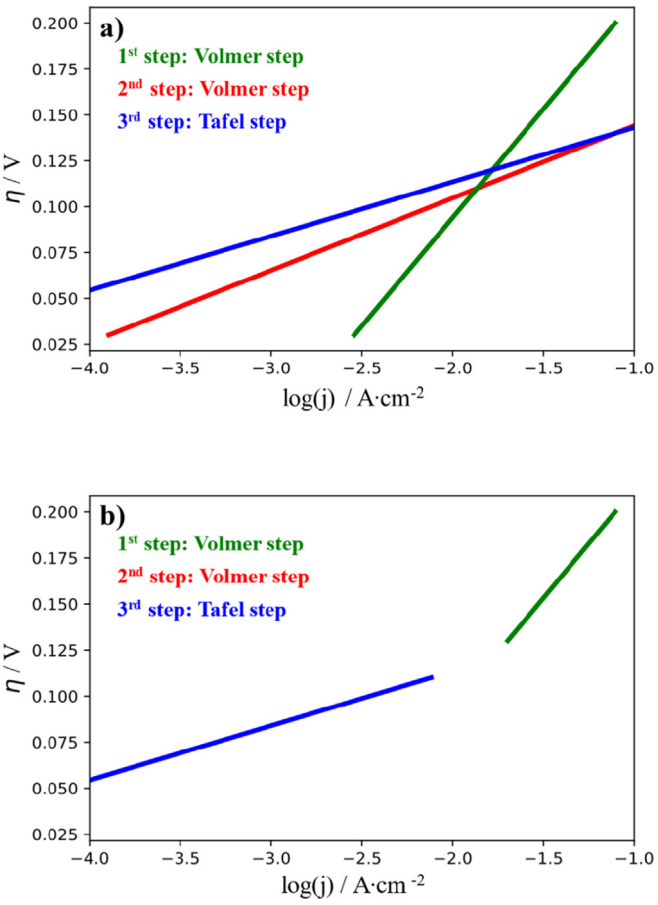


Fig. 5. Schematic representation of linear Tafel regimes for an arbitrary chosen Volmer-Tafel mechanism. While in a) the linear regimes derived from all the three steps of the mechanism are depicted, and b) shows the final Tafel plot. Green, red, and blue lines indicate the current density in dependence of the applied overpotential for each elementary step. In the present figure, the 3rd step, in blue, governs the kinetics of the reaction for small overpotentials (η < 0.1 V) whereas the 1st step, in green, is reconciled with the kinetic bottleneck for larger overpotentials (η > 0.13 V). Consequently, the Tafel plot of the V-T mechanism consists of two linear regimes. The transition between the two linear regimes, indicating a change in the rate-determining step, is not captured by the quasi-equilibrium assumption. (For interpretation of the references to colour in this figure legend, the reader is referred to the web version of this article.)

$$\Delta E_{ZPE} = ZPE_n - ZPE_{n-1}, \tag{25}$$

or,

$$\Delta E_{ZPE}^{\#} = ZPE_n^{\#} - ZPE_{n-1}, \tag{26}$$

and similarly, we can obtain the entropy corrections TΔS, see Eqs. (27) and (28);

$$T\Delta S = TS_n - TS_{n-1}, \tag{27}$$

or,

$$T\Delta S^{\#} = TS_n^{\#} - TS_{n-1}. \tag{28}$$

The entropy containing term in Eqs. (27) and (28) is computed by Eq. (29) [61];

$$TS = k_B N_A T \sum_i^n \frac{h\nu_i/k_BT}{e^{h\nu_i/k_BT}-1} - ln(1-e^{-h\nu_i/k_BT}), \tag{29}$$

where besides the variables described already in Eq. (21), N_A is the Avogadro number and ν_i correspond to the vibrational frequencies of the same normal modes considered in the ZPE calculation.

While the DFT calculations are performed for zero electrode potential, we make use of the computational hydrogen electrode (CHE) [89] approach, to describe the potential dependence on the RHE scale. This framework couples the total energy, the zero-point energy, and entropy of the hydrated proton and electron to half of the free energy of a gaseous H_2 molecule. This equilibrium is met for a pressure of 1 bar of H_2 in a solution of protons with activity 1 at 298.15 K:

$$H^+_{(aq)} + e^- \rightleftharpoons \frac{1}{2}H_{2(g)}, \quad @U = 0V \ vs.\ RHE, \tag{30}$$

since in equilibrium $\Delta G = 0$ is fulfilled, it can be concluded:

$$G\left(H^+_{(aq)}\right) + G(e^-) = \frac{1}{2}G(H_{2(g)}). \tag{31}$$

Based on the introduced framework, application of Eq. (21) allows compiling Tafel plots for the different HER mechanisms. Note that to compute the Tafel plot, positive values of the current density j, are required due to its logarithmic representation in the Tafel plot. Thus, we recall that we use the absolute values of the current density and applied overpotential for the discussion of the elementary processes in the HER in the following.

Finally, a comment is needed on the description of the electrochemical environment within the DFT calculations. While canonical DFT calculations may inappropriately capture free-energy differences by comparing initial, transition, and final states at constant charge instead of constant potential [90], the grand canonical framework may require the evaluation of surface phases with varying H* coverage to keep the electrode potential constant [91]. Since our MXene phases are fully hydrogenated under acidic HER conditions, the approach of a varying H* coverage is not applicable to reach constant potential conditions. Note also that many of the recent theoretical studies still apply constant charge calculations and use a correction term to reach a constant potential description [90,92,93]. Given that there is no consensus in the literature on the aptitude and error bars of the various modifications proposed, we stay with the canonical formalism even if this does not represent the electrochemical environment. However, this methodology allows resolving the HER kinetics in a qualitative fashion, and the derived conclusions in our manuscript are robust due to the significant free-energy differences between the -H* and –OH* covered surfaces.

5. Results and discussion

To simplify the discussion, the results for V_2C-H and V_2C-OH are presented separately and, for each case, the different mechanisms are discussed one after the other.

5.1. The V_2C-H case

We start by considering the Volmer Heyrovsky I (VH-I) path by recalling its mechanistic description according to Eqs. (32) and (33):

$$Volmer\ step: \ H_3O^+ + e^- + M* \rightleftharpoons M-H \ + \ H_2O, \tag{32}$$

$$Heyrovsky\ step: \ H_3O^+ + e^- + M-H \rightleftharpoons M* + H_2 + H_2O. \tag{33}$$

In Eqs. (32) and (33), M* indicates a vacant top site at the water covered V_2C-H surface. In the first step, one hydrogen is adsorbed at the top site on the surface, see Eq. (32), and subsequently, a second hydrogen recombines with the adsorbed H atom at the top site to form the final hydrogen molecule, see Eq. (33). This mechanism is only possible for the V_2C-H system because the top sites on the V_2C-OH surface are sterically hindered.

We discuss in the Supplementary Data (SD) that, in principle, hydrogen could also be adsorbed on HollowC as adsorption site, see Fig. S1 of the SD. Using the unit cell described in Section 2, a total of eighteen initial different adsorption sites were evaluated, including direct and indirect adsorptions; see additional details in Figs. S2-S4 of the SD. Direct adsorptions imply that one hydrogen atom from the H_3O^+ adsorbs in a single step on the respective site. In contrast, indirect adsorption involves two steps in that one H from the H_3O^+ moves toward a vicinal water molecule first, and in a second step, the hydrogen atom pointing towards the surface of the acceptor water molecule is adsorbed at the surface.

Our thermodynamic analysis indicates that the RI, adsorbed hydrogen, appears to be more stable when bound to the top site (adsorption free energies ranging from −0.17 to +0.19 eV) rather than on the HollowC site (adsorption free energy of about 0.30 eV; see Table S1 in the SD). When the water layer is rearranged in response to adsorption, there are several situations where one oxygen atom from the water layer interacts with one V atom from the surface. As the adsorption at the HollowC sites is consistently less energetically favoured than at the top sites, one direct and one indirect HollowC paths are further tested, but we do not find any important differences in terms of the thermodynamic picture. Therefore, hydrogen adsorption on the HollowC site is not further pursued.

Finally, a second hydrogen atom is added to the water layer. This hydrogen atom recombines with the hydrogen species adsorbed on the top site in the Heyrovsky step, and the energetics of the TS, see Tables S2 and S3 in the SD, is quantified following the same procedure as for the Volmer step. Fig. 6 depicts the free-energy diagram of the VH-I mechanism at η = 0 V and 0.2 V. Given that the Volmer step reveals higher TS free energy than the Heyrovsky step at η = 0 V, the Volmer step is reconciled with the rate-determining step, even if the applied overpotential is enhanced. Consequently, the computational Tafel plot reveals a single linear regime as shown in Fig. 7.

Next, we have tested the Volmer-Tafel I (VT-I) over the V_2C-H surface, and its mechanistic description is given by Eqs. (34)–(36):

$$Volmer\ step: \ H_3O^+ + e^- + M* \rightleftharpoons M-H \ + H_2O, \tag{34}$$

$$Volmer\ step: \ H_3O^+ + e^- + M-H \ + \ M* \rightleftharpoons 2(M-H) \ + \ H_2O, \tag{35}$$

$$Tafel\ step: \ 2(M-H) \rightleftharpoons 2M* \ + H_2. \tag{36}$$

While the Volmer steps of Eqs. (32) and (34) are identical, in contrast to the above-discussed VH-I mechanism, the second step contains the adsorption of a second hydrogen atom (*cf.* Eq. (35)). Finally, the two adsorbed hydrogen species recombine under the

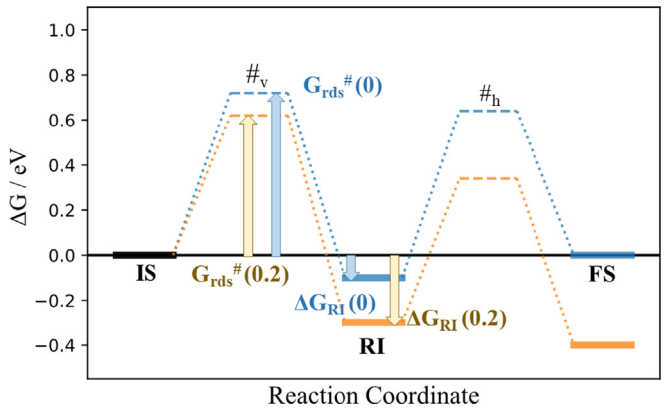


Fig. 6. Free-energy diagram for the VH-I mechanism over the V_2C-H surface at η = 0 V and η = 0.2 V in blue and orange, respectively. While the initial state (IS) is depicted in black, the reaction intermediate (RI) and final state (FS) are indicated by blue solid lines. Transition states (TS) are marked by dashed lines. (For interpretation of the references to colour in this figure legend, the reader is referred to the web version of this article.)

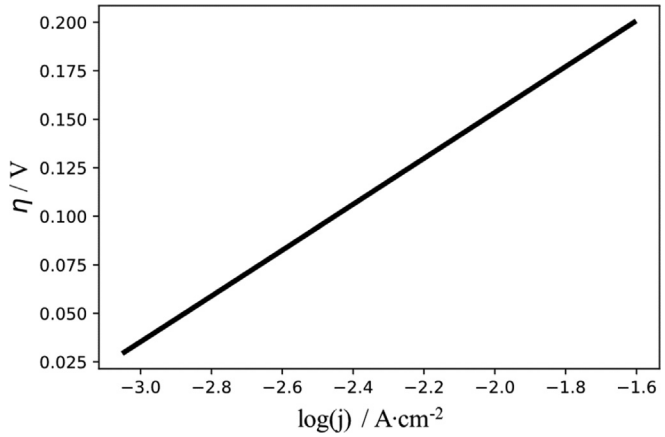


Fig. 7. Simulated Tafel plot of the HER over V_2C-H via the Volmer-Heyrovsky mechanism as obtained from the free-energy landscape of Fig. 6. Given that the first transition state of the mechanism is higher in free energy than the second transition state, the mechanism is limited by a single step, and hence, the Tafel plot reveals a single linear regime.

formation of gaseous hydrogen in the Tafel step (*cf.* Eq. (36)). We recall that the above mechanistic description can only occur on the V_2C-H surface, but cannot take place on the V_2C-OH phase.

The RIs of the VT-I mechanism are reconciled with one hydrogen atom (RI1) or two hydrogen atoms (RI2) adsorbed at the top site. The energetics of the first Volmer step, including the free energies of RI1 and the TS1, can be directly taken from the VH mechanism. Regarding the second Volmer Step, the number of possible pathways increases exponentially as each single RI from the previous mechanism can be taken as a starting point. Therefore, several Top and HollowC sites, including direct and indirect adsorption, are evaluated. Figs S5-S7 of the SD show the adsorption sites tested for the first and second Volmer steps, respectively, and data is encompassed in Tables S4-S6 of the SD.

It turns out that hydrogen adsorption at the Top site is energetically preferred over the HollowC site. However, a second hydrogen atom on the surface results in a less favourable adsorption energetics compared to the first Volmer step, revealing adsorption free energies of 0.30 to 0.56 eV. We note that the repulsion of adjacent hydrogen species on solid-state electrodes is well documented in the literature [94]. The kinetic barriers for the Tafel step, however, are surprisingly small, given that these are in the range of 0.32 to 0.61 eV, especially in comparison with the formation barriers of hydrogen on bare MXenes [59]. This can be explained by referring to the surface termination: For V_2C-H, the most stable sites of H adsorption (HollowM) are already occupied by hydrogen. Consequently, the less stable top adsorption sites are involved in the formation of the hydrogen molecule, and this leads to a facile kinetics.

Fig. 8 shows the Gibbs free energy diagram of the VT-I mechanism at η = 0 V and 0.2 V. Both Volmer step TSs require similar barriers, but the second barrier is slightly higher, implying that for low overpotentials, the rate-determining step refers to the second Volmer step. However, when gradually increasing the overpotential, the first Volmer step is reconciled with the kinetic bottleneck. Thus, the Tafel plot for the VT-I mechanism consists of two lineal regimes where the kinetics of the reaction are dominated by the second and first Volmer steps (*cf.* Fig. 9).

The last mechanism tested over the V_2C-H surface refers to an alternative Volmer-Tafel mechanism (VT-II). Essentially, this mechanism corresponds to the initial VT description, but the order between the Volmer and Tafel steps is changed:

$$\textit{Volmer step}: \quad H_3O^+ + e^- + M* \rightleftharpoons M-H + H_2O, \tag{37}$$

$$\textit{Tafel step}: \quad M-H + H_{HM} \rightleftharpoons M'* + H_2, \tag{38}$$

$$\textit{Volmer step}: \quad H_3O^+ + e^- + M'* \rightleftharpoons H_{HM} + H_2O. \tag{39}$$

The first step in Eq. (37) is identical to the two previous mechanisms. Yet, the adsorbed hydrogen species directly recombines with another hydrogen from the HollowM site —H_{HM} in Eq. (38)— to release a hydrogen molecule (*cf.* Eq. (38)). Finally, the resulting vacancy on the HollowM site is filled up by hydrogen again (*cf.* Eq. (39)). Please, note that M′* stands for the MXene surface with a free HollowM site.

Our calculations reveal though that the Tafel step is blocked. This is mainly related to the fact that hydrogen on the HollowM site is strongly bound, and this majorly hampers the HER kinetics. Therefore, this mechanistic description is not further pursued.

5.2. The V_2C-OH case

The HER over the V_2C-OH surface can occur via the Volmer Heyrovsky mechanism, but here the steps are inverted, and thus, this mechanism is denoted as VH-II.

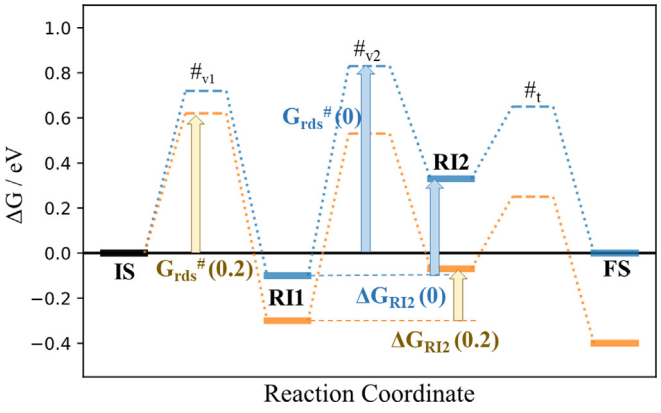


Fig. 8. Free-energy diagram for the Volmer-Tafel mechanism at η = 0 V and η = 0.2 V in blue and orange, respectively. While the initial state (IS) is depicted in black, the reaction intermediate (RI) and final state (FS) are indicated by blue solid lines. Transition states (TS) are marked by dashed lines. (For interpretation of the references to colour in this figure legend, the reader is referred to the web version of this article.)

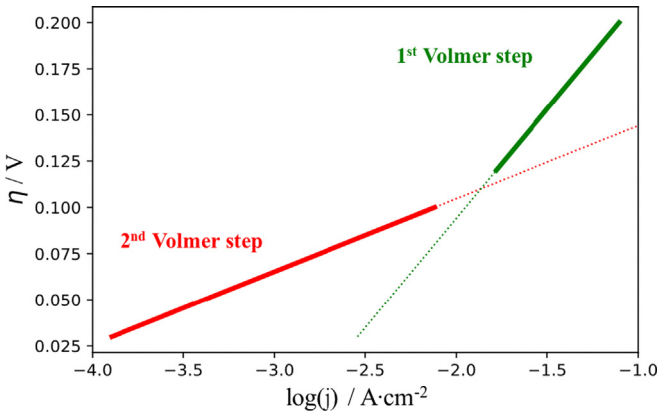


Fig. 9. Simulated Tafel plot of the HER over V_2C-H *via* the Volmer-Tafel mechanism as obtained from the free-energy landscape of Fig. 8. Two linear regimes are obtained in that the second Volmer steps limits the rate for small overpotentials whereas the first Volmer step becomes rate determining for large overpotentials.

$$\textit{Heyrovsky step}: \quad H_3O^+ + e^- + MO - H \rightleftharpoons MO* + H_2 + H_2O \tag{40}$$

$$\textit{Volmer step}: \quad H_3O^+ + e^- + MO* \rightleftharpoons MO - H + H_2O. \tag{41}$$

First, one hydrogen from the water layer recombines with adsorbed hydrogen from the OH adsorbates on the HollowM sites to form gaseous hydrogen in the Heyrovsky step (*cf.* Eq. (40)). Thereafter, one hydrogen atom from the electrolyte replaces the missing hydrogen atom in the Volmer step (*cf.* Eq. (41)). Consequently, the RI in this mechanism is reconciled with surface oxygen, MO*. We note that, for the water ice-like layer, we have used the same initial configuration as for V_2C-H, but the final configuration differs slightly upon relaxation. Four different reaction paths have been considered, which are summarized in Fig. S8 of the SD.

The RIs for all four paths are extremely stable in comparison to the IS, $\Delta G \sim$ -3.45 eV. Therefore, regardless of any kinetic barrier this mechanism can already be excluded based on thermodynamic reasoning, and thus, is no longer explored.

Finally, the last evaluated pathway corresponds to a third variant of the Volmer Tafel mechanism (VT-III).

$$\textit{Tafel step}: \quad MO - H* + MO - H* \rightleftharpoons 2MO* + H_2 \tag{42}$$

$$\textit{Volmer step}: \quad H^+ + e^- + 2MO* \rightleftharpoons MO - H* + MO*. \tag{43}$$

$$\textit{Volmer step}: \quad H^+ + e^- + MO* + MO - H* \rightleftharpoons 2MO - H*. \tag{44}$$

Here, two hydrogen atoms from the OH terminating groups recombine *via* a Tafel step to form gaseous hydrogen (*cf.* Eq. (42)), and afterwards, two hydrogen atoms adsorb on the O-covered moieties to close the catalytic cycle (*cf.* Eqs. (43) and (44)). In this case, the RIs are reconciled with 2 MO* and MO* plus a MO-H*.

Our calculations reveal that the free-energy barrier for the initial Tafel step (about 1.43 eV) is the highest among all investigated barriers studied. Therefore, $G^{\#}_{rds}$ for this mechanism is twice as large as for the VH-I and VT-I mechanisms, and thus, is not further considered.

5.3. Comparison of active sites and mechanisms

In summary, we have investigated the HER kinetics over the V_2C-H and V_2C-OH surfaces. Our DFT calculations clearly indicate that V_2C-H corresponds to the active site motif under HER conditions in that the vacant top sites are responsible for the formation of gaseous hydrogen. This is an important information given that HollowM rather than Top corresponds to the energetically preferred adsorption site of V_2C under HER conditions. Using thermodynamic considerations by determining the free energy of adsorbed hydrogen only would likely result in an incorrect result since the hydrogen bond strength on the energetically favoured HollowM site would be evaluated, and this binding energy cannot be related *via* BEP relation to the kinetics of the HER over the top sites, as resolved in this study. This finding emphasizes the danger of hasty conclusions by thermodynamic approaches and equally underpins the importance of kinetic studies to resolve the entire free-energy landscape.

Relating to the V_2C-H surface, we have demonstrated that two mechanistic descriptions are possible, namely the VH-I and VT-I pathways. Fig. 10 shows a comparison of the Tafel plot for the two mechanistic descriptions. While for small overpotentials the VH-I mechanism is energetically preferred, it is evident that for larger overpotentials the VT-I pathway is kinetically favoured. This finding can be explained by the fact that with increasing overpotential, the coverage of adsorbed hydrogen on the top site increases, which facilitates the chemical recombination of two adjacent hydrogen atoms on the top sites compared to the electrochemical Heyrovsky step in the VH-I mechanism. Note that the overall qualitative picture remains unaltered when increasing or decreasing α values to 0.3 or 0.7, see Fig. S9 of the SD, with only slight changes in the exact overpotential of transitioning between determining reaction. The obtained results in terms of the top sites as active species for the HER and the Volmer-Tafel mechanism as the preferred mechanistic description for large overpotentials is somewhat reminiscent of the HER over Pt(1 1 1) [62,95], and this may be another cornerstone why MXenes are promising electrocatalysts for the generation of hydrogen. Especially, because MXenes are 2D versions of transition metal carbide materials [96], which are known to behave like Pt-group metals in catalysis [97].

Finally, by comparing the Tafel plots of the VH-I and VT-I mechanism with an experimentally reported Tafel plot of the HER over V_2C, we observe the impact of the MXene termination (OH– *vs.* H-covered surface) on the electrocatalytic performance. The experimentally reported Tafel plot [98] indicates that V_2C is not active toward the HER in the potential regime of -0.5 V < U *vs.*

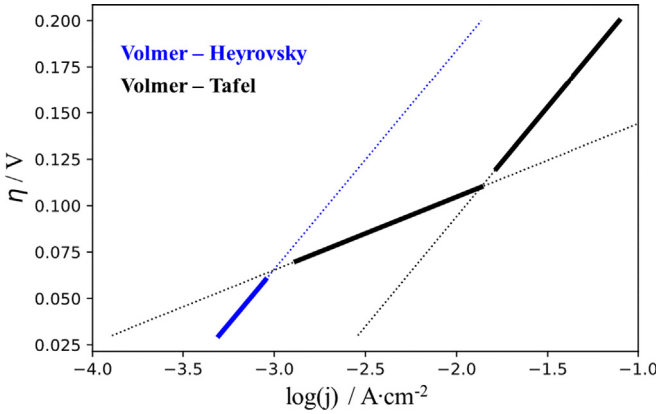


Fig. 10. Simulated Tafel plots of the HER over V_2C-H *via* the Volmer-Heyrovsky and Volmer-Tafel mechanisms in blue and black, respectively as obtained from the free-energy landscape of Figs. 6 and 8. For small applied overpotential, η 0.07 V, the Volmer- Heyrovsky mechanism is kinetically preferred whereas for larger overpotentials the Volmer-Tafel mechanism describes the reaction rate. (For interpretation of the references to colour in this figure legend, the reader is referred to the web version of this article.)

RHE < 0 V. We trace this finding to the presence of the OH-covered surface under these potential conditions (*cf.* Section 2), given that we demonstrated that the HER kinetics of this surface termination is poor. On the contrary, the experimental Tafel plot indicates hydrogen formation for U < -0.5 V *vs.* RHE, and this can be explained by the presence of the H-covered surface, which has a facile kinetics according to our first-principles study. Consequently, the HER kinetics of V_2C can be tuned if the transition from the kinetically inactive OH* phase to the active H* phase is shifted toward more positive potentials and ideally occurs at about $U = 0$ V *vs.* RHE.

6. Conclusions

Taking V_2C (0001) as a representative case of the MXene family, five different hydrogen evolution reaction (HER) mechanisms have been studied for two different surface terminations, which are chosen based on the Pourbaix diagram under HER conditions. The V_2C (0001) surface is either covered by H* or OH* on HollowM sites, and we explicitly account for the presence of water by considering an ice-like monolayer in our simulations.

The present study pinpoints that, despite the availability of a plethora of hydrogen adsorbates on the V_2C surface, the HER is more complex than initially thought. We demonstrate that the OH* termination does not show catalytic activity toward hydrogen formation but rather the H-covered surface corresponds to the active motif under HER conditions. However, the active hydrogen atoms adsorb on the unoccupied top sites and are not reconciled with the energetically preferred HollowM site. We study the Volmer-Heyrovsky and Volmer-Tafel mechanisms over the H-covered surface, construct free-energy diagrams by resolving the thermodynamics (reaction intermediates) and kinetics (transition states) from density functional theory (DFT), and compile Tafel plots by applying a rigorous microkinetic framework.

Our simulations reveal that the Volmer-Heyrovsky pathway corresponds to the preferred mechanistic description for small overpotentials whereas the Volmer-Tafel path becomes kinetically preferred for larger overpotentials. The obtained results are surprisingly similar to the HER over Pt, thus providing evidence why MXenes are potential electrocatalysts for the formation of gaseous hydrogen by means of electrochemical water splitting. Also, our combined approach consisting of DFT calculations and microkinetic considerations may serve as a guideline of how to unravel the elementary steps of electrocatalytic processes, such as for the HER, by moving beyond the prototypical thermodynamic framework focusing on adsorption free energies only.

Data availability

Data will be made available on request.

Declaration of Competing Interest

The authors declare that they have no known competing financial interests or personal relationships that could have appeared to influence the work reported in this paper.

Acknowledgements

The research carried out at the *Universitat de Barcelona* has been supported by the Spanish MCIN/AEI/10.13039/501100011033 PID2021-126076NB-I00 project, funded partially by FEDER *Una manera de hacer Europa*, and *María de Maeztu* CEX2021-001202-M grants, including funding from European Union and, in part, by and COST Action CA18234. A significant part of the computational resources has been provided by the *Red Española de Supercomputación* (RES) QS-2020-2-0004 and QS-2020-1-0011. M.L. thanks *Universitat de Barcelona* for an APIF predoctoral contract, the HPC-EUROPA3 (INFRAIA-2016-1-730897) project supported by the EC Research Innovation Action under the H2020 Programme, the University of Duisburg-Essen and the High Performance Computing Center Stuttgart (HRLS) for supporting his stay in Essen. K.S.E. acknowledges funding by the Ministry of Culture and Science of the Federal State of North Rhine-Westphalia (NRW Return Grant). K.S.E. is associated with the CRC/TRR247: "Heterogeneous Oxidation Catalysis in the Liquid Phase" (Project number 388390466-TRR 247), the RESOLV Cluster of Excellence, funded by the Deutsche Forschungsgemeinschaft under Germany's Excellence Strategy – EXC 2033-390677874 – RESOLV, and the Center for Nanointegration (CENIDE).

Appendix A. Supplementary material

Supplementary data to this article can be found online at https://doi.org/10.1016/j.jcat.2023.03.027.

References

[1] UN Doc FCCC/CP/1997/7/Add.1. Kyoto Protocol to the United Nations Framework Convention on Climate Change Dec. 10, 1997; 37 ILM 22 1998.
[2] UN Doc FCCC/CP/2009/L.7, Copenhagen Accord.18 December 2009.
[3] UN Doc FCCC/CP/2015/7, Paris Agreement, 2015.
[4] UN Doc FCCC/CP/2021/L.13, Glasgow Climate Pact, 2021.
[5] Iea, Global Energy Review 2021, IEA, Paris, 2021.
[6] S. Chu, A. Majumdar, Opportunities and Challenges for a Sustainable Energy Future, Nature 488 (2012) 294–303.
[7] D.G. Nocera, N.S. Lewis, Powering the planet: chemical challenges in solar energy utilization, Proc. Natl. Acad. Sci. 103 (2006) 15729–15735.
[8] I. Dincer, C. Zamfirescu, Sustainable Hydrogen Production; Elsevier, Ed.; 2016.
[9] G.W. Crabtree, M.S. Dresselhaus, M.V. Buchanan, The hydrogen economy, Phys. Today 57 (2004) 39–44.
[10] Y. Li, W. Liu, Z. Zhang, X. Du, L. Yu, Y. Deng, A self-powered electrolytic process for glucose to hydrogen conversion, Commun. Chem. 2 (2019) 1–9.
[11] X. Gao, H. Zhang, Q. Li, X. Yu, Z. Hong, X. Zhang, C. Liang, Z. Lin, Hierarchical $NiCo_2O_4$ hollow microcuboids as bifunctional electrocatalysts for overall water-splitting, Angew. Chemie - Int. Ed. 55 (2016) 6290–6294.
[12] J. Wang, Y. Gao, D. Chen, J. Liu, Z. Zhang, Z. Shao, F. Ciucci, Water splitting with an enhanced bifunctional double perovskite, ACS Catal. 8 (2018) 364–371.
[13] P. Du, R. Eisenberg, Catalysts made of earth-abundant elements (Co, Ni, Fe) for water splitting: recent progress and future challenges, Energy Environ. Sci. 5 (2012) 6012–6021.
[14] J.N. Hansen, H. Prats, K.K. Toudahl, N. Mørch Secher, K. Chan, J. Kibsgaard, I. Chorkendorff, Is there anything better than Pt for HER?, ACS Energy Lett (2021) 1175–1180.
[15] S.J. Gutić, A.S. Dobrota, E. Fako, N.V. Skorodumova, N. López, I.A. Pašti, Hydrogen evolution reaction-from single crystal to single atom catalysts, Catalysts 10 (2020) 290.
[16] M. Tahir, L. Pan, F. Idrees, X. Zhang, L. Wang, J.J. Zou, Z.L. Wang, Electrocatalytic oxygen evolution reaction for energy conversion and storage: a comprehensive review, Nano Energy 37 (2017) 136–157.
[17] B. Samanta, Á. Morales-García, F. Illas, N. Goga, J.A. Anta, S. Calero, A. Bieberle-Hütter, F. Libisch, A.B. Muñoz-García, M. Pavone, M. Caspary Toroker, Challenges of modeling nanostructured materials for photocatalytic water splitting, Chem. Soc. Rev. 51 (2022) 3794–3818.
[18] Y. Zhong, X. Xia, F. Shi, J. Zhan, J. Tu, H.J. Fan, Transition metal carbides and nitrides in energy storage and conversion, Adv. Sci. 3 (2016) 1500286.
[19] W.F. Chen, J.T. Muckerman, E. Fujita, Recent developments in transition metal carbides and nitrides as hydrogen evolution electrocatalysts, Chem. Commun. 49 (2013) 8896–8909.
[20] W.F. Chen, C.H. Wang, K. Sasaki, N. Marinkovic, W. Xu, J.T. Muckerman, Y. Zhu, R.R. Adzic, Highly active and durable nanostructured molybdenum carbide electrocatalysts for hydrogen production, Energy Environ. Sci. 6 (2013) 943–951.
[21] D. Voiry, H. Yamaguchi, J. Li, R. Silva, D.C.B. Alves, T. Fujita, M. Chen, T. Asefa, V. B. Shenoy, G. Eda, M. Chhowalla, Enhanced catalytic activity in strained chemically exfoliated WS_2 nanosheets for hydrogen evolution, Nat. Mater. 12 (2013) 850–855.
[22] L. Wu, A.J.F. van Hoof, N.Y. Dzade, L. Gao, M.-I. Richard, H. Friedrich, N.H. de Leeuw, E.J.M. Hensen, J.P. Hoffman, Enhancing the electrocatalytic activity of 2H-WS_2 for hydrogen evolution via defect engineering, Phys. Chem. Chem. Phys. 21 (2019) 6071–6079.

[23] T.F. Jaramillo, K.P. Jørgensen, J. Bonde, J.H. Nielsen, S. Horch, I. Chorkendorff, Identification of active edge sites for electrochemical H_2 evolution from MoS_2 nanocatalysts, Science 317 (2007) 100–102.
[24] E.J. Popczun, C.G. Read, C.W. Roske, N.S. Lewis, R.E. Schaak, Highly active electrocatalysis of the hydrogen evolution reaction by cobalt phosphide nanoparticles, Angew. Chemie - Int. Ed. 53 (2014) 5427–5430.
[25] H. Yoon, H.J. Song, B. Ju, D.W. Kim, Cobalt phosphide nanoarrays with crystalline-amorphous hybrid phase for hydrogen production in universal-PH, Nano Res. 13 (2020) 2469–2477.
[26] E.J. Popczun, J.R. McKone, C.G. Read, A.J. Biacchi, A.M. Wiltrout, N.S. Lewis, R.E. Schaak, Nanostructured nickel phosphide as an electrocatalyst for the hydrogen evolution reaction, J. Am. Chem. Soc. 135 (2013) 9267–9270.
[27] L. Liu, Q. Xu, Q. Zhu, Electrically conductive metal-organic frameworks for electrocatalytic applications, Adv. Energy Sustain. Res. 2 (2021) 2100100.
[28] R. Dong, M. Pfeffermann, H. Liang, Z. Zheng, X. Zhu, J. Zhang, X. Feng, Large-area, free-standing, two-dimensional supramolecular polymer single-layer sheets for highly efficient electrocatalytic hydrogen evolution, Angew. Chemie - Int. Ed. 54 (2015) 12058–12063.
[29] A.J. Clough, J.W. Yoo, M.H. Mecklenburg, S.C. Marinescu, Two-dimensional metal-organic surfaces for efficient hydrogen evolution from water, J. Am. Chem. Soc. 137 (2015) 118–121.
[30] Y. Gogotsi, B. Anasori, The Rise of MXenes, ACS Nano 13 (2019) 8491–8494.
[31] Á. Morales-García, F. Calle-Vallejo, F. Illas, MXenes: new horizons in catalysis, ACS Catal. 10 (2020) 13487–13503.
[32] M. Naguib, O. Mashtalir, J. Carle, V. Presser, J. Lu, L. Hultman, Y. Gogotsi, M.W. Barsoum, Two-dimensional transition metal carbides, ACS Nano 6 (2012) 1322–1331.
[33] M. Naguib, M.W. Barsoum, Y. Gogotsi, Ten years of progress in the synthesis and development of MXenes, Adv. Mater. 33 (2021) 2103393.
[34] J.D. Gouveia, Á. Morales-García, F. Viñes, J.R.B. Gomes, F. Illas, MXenes à La Carte: tailoring the epitaxial growth alternating nitrogen and transition metal layers, ACS Nano 16 (2022) 12541–12552.
[35] S. Liu, Z. Song, X. Jin, R. Mao, T. Zhang, F. Hu, MXenes for metal-ion and metal-sulfur batteries: synthesis, properties, and electrochemistry, Mater. Reports Energy 2 (2022).
[36] X. Liang, A. Garsuch, L.F. Nazar, Sulfur cathodes based on conductive MXene nanosheets for high-performance lithium-sulfur batteries, Angew. Chemie - Int. Ed. 54 (2015) 3907–3911.
[37] X. Wang, S. Kajiyama, H. Iinuma, E. Hosono, S. Oro, I. Moriguchi, M. Okubo, A. Yamada, Pseudocapacitance of MXene nanosheets for high-power sodium-ion hybrid capacitors, Nat. Commun. 6 (2015) 6544.
[38] K. Rasool, M. Helal, A. Ali, C.E. Ren, Y. Gogotsi, K.A. Mahmoud, Antibacterial activity of $Ti_3C_2T_x$ MXene, ACS Nano 10 (2016) 3674–3684.
[39] R. Morales-Salvador, Á. Morales-García, F. Viñes, F. Illas, Two-dimensional nitrides as highly efficient potential candidates for CO_2 capture and activation, Phys. Chem. Chem. Phys. 20 (2018) 17117–17124.
[40] Á. Morales-García, A. Fernández-Fernández, F. Viñes, F. Illas, CO_2 abatement using two-dimensional MXene carbides, J. Mater. Chem. A 6 (2018) 3381–3385.
[41] I. Persson, J. Halim, H. Lind, T.W. Hansen, J.B. Wagner, L.Å. Näslund, V. Darakchieva, J. Palisaitis, J. Rosen, P.O.Å. Persson, 2D transition metal carbides (MXenes) for carbon capture, Adv. Mater. 31 (2019) 1805472.
[42] N. Li, X. Chen, W.J. Ong, D.R. Macfarlane, X. Zhao, A.K. Cheetham, C. Sun, Understanding of electrochemical mechanisms for CO_2 capture and conversion into hydrocarbon fuels in transition-metal carbides (MXenes), ACS Nano 11 (2017) 10825–10833.
[43] A.D. Handoko, S.N. Steinmann, Z.W. Seh, Theory-guided materials design: two-dimensional MXenes in electro- and photocatalysis, Nanoscale Horizons 4 (2019) 809–827.
[44] P. Hou, Y. Tian, D. Jin, X. Liu, Y. Xie, F. Du, X. Meng, Advances in theoretical calculations of MXenes as hydrogen and oxygen evolution reaction (water splitting) electrocatalysts, J. Phys. D. Appl. Phys. 55 (2022).
[45] M.P. Browne, D. Tyndall, V. Nicolosi, The potential of MXene materials as a component in the catalyst layer for the oxygen evolution reaction, Curr. Opin. Electrochem. 34 (2022).
[46] Z.W. Seh, K.D. Fredrickson, B. Anasori, J. Kibsgaard, A.L. Strickler, M.R. Lukatskaya, Y. Gogotsi, T.F. Jaramillo, A. Vojvodic, Two-dimensional molybdenum carbide (MXene) as an efficient electrocatalyst for hydrogen evolution, ACS Energy Lett. 1 (2016) 589–594.
[47] J.K. Nørskov, T. Bligaard, A. Logadottir, J.R. Kitchin, J.G. Chen, S. Pandelov, U. Stimming, Trends in the exchange current for hydrogen evolution, J. Electrochem. Soc. 152 (2005) J23.
[48] C. Ling, L. Shi, Y. Ouyang, J. Wang, Searching for highly active catalysts for hydrogen evolution reaction based on O-terminated MXenes through a simple descriptor, Chem. Mater. 28 (2016) 9026–9032.
[49] D. Jin, L.R. Johnson, A.S. Raman, X. Ming, Y. Gao, F. Du, Y. Wei, G. Chen, A. Vojvodic, Y. Gogotsi, X. Meng, Computational screening of 2D ordered double transition-metal carbides (MXenes) as electrocatalysts for hydrogen evolution reaction, J. Phys. Chem. C 124 (2020) 10584–10592.
[50] M. Pandey, K.S. Thygesen, Two-dimensional MXenes as catalysts for electrochemical hydrogen evolution: a computational screening study, J. Phys. Chem. C 121 (2017) 13593–13598.
[51] Z. Kang, M.A. Khan, Y. Gong, R. Javed, Y. Xu, D. Ye, H. Zhao, J. Zhang, Recent progress of MXenes and MXene-based nanomaterials for the electrocatalytic hydrogen evolution reaction, J. Mater. Chem. A 9 (2021) 6089–6108.
[52] A.D. Handoko, K.D. Fredrickson, B. Anasori, K.W. Convey, L.R. Johnson, Y. Gogotsi, A. Vojvodic, Z.W. Seh, Tuning the basal plane functionalization of two-dimensional metal carbides (MXenes) to control hydrogen evolution activity, ACS Appl. Energy Mater. 1 (2018) 173–180.
[53] G. Gao, A.P. O'Mullane, A. Du, 2D MXenes: a new family of promising catalysts for the hydrogen evolution reaction, ACS Catal. 7 (2017) 494–500.
[54] K.S. Exner, H. Over, Kinetics of electrocatalytic reactions from first-principles: a critical comparison with the ab initio thermodynamics approach, Acc. Chem. Res. 50 (2017) 1240–1247.
[55] K.S. Exner, Does a thermoneutral electrocatalyst correspond to the apex of a volcano plot for a simple two-electron process?, Angew Chemie - Int. Ed. 59 (2020) 10236–10240.
[56] J.R.B. Gomes, J.M. Bofill, F. Illas, Azomethane decomposition catalyzed by Pt (111): an example of anti-brönsted-evans-polanyi behavior, J. Phys. Chem. C 112 (2008) 1072–1080.
[57] E.V. Miu, J.R. McKone, G. Mpourmpakis, The sensitivity of metal oxide electrocatalysis to bulk hydrogen intercalation: hydrogen evolution on tungsten oxide, J. Am. Chem. Soc. 144 (2022) 6420–6433.
[58] J.D. Gouveia, Á. Morales-García, F. Viñes, F. Illas, J.R.B. Gomes, MXenes as promising catalysts for water dissociation, Appl. Catal. B Environ. 260 (2020).
[59] M. López, Á. Morales-García, F. Viñes, F. Illas, Thermodynamics and kinetics of molecular hydrogen adsorption and dissociation on MXenes: relevance to heterogeneously catalyzed hydrogenation reactions, ACS Catal. 11 (2021) 12850–12857.
[60] J.D. Gouveia, Á. Morales-García, F. Viñes, J.R.B. Gomes, F. Illas, Facile heterogeneously catalyzed nitrogen fixation by MXenes, ACS Catal. 10 (2020) 5049–5056.
[61] M. López, K.S. Exner, F. Viñes, F. Illas, Computational pourbaix diagrams for MXenes: a key ingredient toward proper theoretical electrocatalytic studies, Adv. Theory Simul. (2022) 2200217.
[62] P. Lindgren, G. Kastlunger, A.A. Peterson, A challenge to the G ~0 interpretation of hydrogen evolution. ACS Catal. 10 (2020) 121–128.
[63] M.T. Tang, X. Liu, Y. Ji, J.K. Nørskov, K. Chan, Modeling hydrogen evolution reaction kinetics through explicit water-metal interfaces, J. Phys. Chem. C 124 (2020) 28083–28092.
[64] P. Hohenberg, W. Kohn, Inhomogeneous electron gas, Phys. Rev. 136 (1964) B864–B871.
[65] W. Kohn, L.J. Sham, Self-consistent equatios including exchange and correlation effects, Phys. Rev. 140 (1965) A1133–A1138.
[66] G. Kresse, J. Hafner, Norm-conserving and ultrasoft pseudopotentials for first-row and transition elements, J. Phys. Condens. Matter 6 (1994) 8245–8257.
[67] G. Kresse, J. Furthmüller, Efficient iterative schemes for ab initio total-enery calculations using a plane-wave basis set, Phys. Rev. B 54 (1996) 11169–11186.
[68] G. Kresse, J. Furthmüller, Efficiency of ab-initio total energy calculations for metals and semiconductors using a plane-wave basis set, Comput. Mater. Sci. 6 (1996) 15–50.
[69] J.P. Perdew, K. Burke, M. Ernzerhof, Generalized gradient approximation made simple, Phys. Rev. Lett. 77 (1996) 3865–3868.
[70] S. Grimme, J. Antony, S. Ehrlich, H. Krieg, A consistent and accurate ab initio parametrization of density functional dispersion correction (DFT-D) for the 94 elements H-Pu, J. Chem. Phys. 132 (2010).
[71] P.E. Blöchl, Projector augmented-wave method, Phys. Rev. B 50 (1994) 17953–17979.
[72] G. Kresse, D. Joubert, From ultrasoft pseudopotentials to the projector augmented-wave method, Phys. Rev. B - Condens. Matter Mater. Phys. 59 (1999) 1758–1775.
[73] R. Morales-Salvador, J.D. Gouveia, Á. Morales-García, F. Viñes, J.R.B. Gomes, F. Illas, Carbon capture and usage by MXenes, ACS Catal. 11 (2021) 11248–11255.
[74] H. Prats, H. McAloone, F. Viñes, F. Illas, Ultra-high selectivity biogas upgrading through porous MXenes, J. Mater. Chem. A 8 (2020) 12296–12300.
[75] Y. Xie, P.R.C. Kent, Hybrid density functional study of structural and electronic properties of functionalized $Ti_{n+1}X_n$ (X = C, N) monolayers, Phys. Rev. B 87 (2013).
[76] J.L.C. Fajín, M.N.D.S. Cordeiro, J.R.B. Gomes, F. Illas, On the need for spin polarization in heterogeneously catalyzed reactions on nonmagnetic metallic surfaces, J. Chem. Theory Comput. 8 (2012) 1737–1743.
[77] G. Henkelman, B.P. Uberuaga, H. Jónsson, Climbing image nudged elastic band method for finding saddle points and minimum energy paths, J. Chem. Phys. 113 (2000) 9901–9904.
[78] A. Heyden, A.T. Bell, F.J. Keil, Efficient methods for finding transition states in chemical reactions: comparison of improved dimer method and partitioned rational function optimization method, J. Chem. Phys. 123 (2005).
[79] K. Momma, F. Izumi, VESTA 3 for three-dimensional visualization of crystal, volumetric and morphology data, J. Appl. Crystallogr. 44 (2011) 1272–1276.
[80] G. Zhong, T. Cheng, A.H. Shah, C. Wan, Z. Huang, S. Wang, T. Leng, Y. Huang, W. A. Goddard III, X. Duan, Determining the hydronium PKα at platinum surfaces and the effect on ph-dependent hydrogen evolution reaction kinetics, Proc. Natl. Acad. Sci. U. S. A. 119 (2022) 1–8.
[81] W. Sheng, H.A. Gasteiger, Y. Shao-Horn, Hydrogen oxidation and evolution reaction kinetics on platinum: acid vs alkaline electrolytes, J. Electrochem. Soc. 157 (2010) B1529.
[82] I. Ledezma-Yanez, W.D.Z. Wallace, P. Sebastián-Pascual, V. Climent, J.M. Feliu, M.T.M. Koper, Interfacial water reorganization as a PH-dependent descriptor of

the hydrogen evolution rate on platinum electrodes, Nat. Energy 2 (2017) 17031.
[83] T. Brülle, O. Schneider, U. Stimming, Fundamental Investigation of the HER on a Pt(111) surface at temperatures down to 120 K, Zeitschrift fur Phys Chemie 226 (2012) 919–934.
[84] R. Guidelli, R.G. Compton, J.M. Feliu, E. Gileadi, J. Lipkowski, W. Schmickler, S. Trassati, Defining the transfer coefficient in electrochemistry: an assessment (IUPAC Technical Report), Pure Appl. Chem. 86 (2014) 245–258.
[85] R. Parsons, General equations for the kinetics of electrode processes, Trans. Faraday Soc. 47 (1951) 1332–1344.
[86] J. Tafel, Über Die Polarisation Bei Kathodischer Wasserstoffentwicklung, Zeitschrift für Phys, Chemie 50 (1905) 641–712.
[87] K.S. Exner, Why the Microkinetic Modeling of Experimental Tafel Plots Requires Knowledge of the Reaction Intermediate's Binding Energy, Electrochem. Sci. Adv. 2 (2021) e2100037.
[88] K.S. Exner, I. Sohrabnejad-Eskan, H. Over, A universal approach to determine the free energy diagram of an electrocatalytic reaction, ACS Catal. 8 (2018) 1864–1879.
[89] J.K. Nørskov, J. Rossmeisl, A. Logadottir, L. Lindqvist, J.R. Kitchin, T. Bligaard, H. Jónsson, Origin of the overpotential for oxygen reduction at a fuel-cell cathode, J. Phys. Chem. B 108 (2004) 17886–17892.
[90] D. Luan, J. Xiao, Adaptive Electric Fields Embedded Electrochemical Barrier Calculations, J. Phys. Chem. Lett. 14 (2023) 685–693.
[91] H. H. Kristoffersen, Modeling Electrochemical Proton Adsorption at Constant Potential with Explicit Charging. ChemCatChem 14 (2022) e202200826.
[92] E. Skúlason, V. Tripkovic, M.E. Björketun, S. Gudmundsdóttir, G. Karlberg, J. Rossmeisl, T. Bligaard, H. Jónsson, J.K. Nørskov, Modeling the electrochemical hydrogen oxidation and evolution reactions on the basis of density functional theory calculations, J. Phys. Chem. C 114 (2010) 18182–18197.
[93] P.S. Lamoureux, A.R. Singh, K. Chan, PH effects on hydrogen evolution and oxidation over Pt(111): insights from first-principles, ACS Catal. 9 (2019) 6194–6201.
[94] A.R. Zeradjanin, J.P. Grote, G. Polymeros, K.J.J. Mayrhofer, A critical review on hydrogen evolution electrocatalysis: re-exploring the volcano-relationship, Electroanalysis 28 (2016) 2256–2269.
[95] R. Kronberg, K. Laasonen, Reconciling the experimental and computational hydrogen evolution activities of Pt(111) through DFT-based constrained MD simulations, ACS Catal. 11 (2021) 8062–8078.
[96] Á. Morales-García, M. Mayans-Llorach, F. Viñes, F. Illas, Thickness biased capture of CO_2 on carbide MXenes, Phys. Chem. Chem. Phys. 21 (2019) 23136–23142.
[97] R.B. Levy, M. Boudart, Platinum-like behavior of tungsten carbide in surface catalysis, Science 181 (1973) 547–549.
[98] Y. Yoon, A.P. Tiwari, M. Choi, T.C. Novak, W. Song, H. Chang, T. Zyung, S.S. Lee, S. Jeon, K.-S. An, Precious-metal-free electrocatalysts for activation of hydrogen evolution with nonmetallic electron donor: chemical composition controllable phosphorous doped vanadium carbide MXene, Adv. Funct. Mater. 29 (2019) 1903443.